11-1-2020

Basis Set Truncation Further Clarifies Vibrational Coherence Spectra

Daniel B. Turner
Boise State University

Paul C. Arpin
California State University, Chico

Publication Information

Turner, Daniel B. and Arpin, Paul C. (2020). "Basis Set Truncation Further Clarifies Vibrational Coherence Spectra". *Chemical Physics, 539*, 110948-1 - 110948-8. https://doi.org/10.1016/j.chemphys.2020.110948

Chemical Physics 539 (2020) 110948

Contents lists available at ScienceDirect

Chemical Physics

journal homepage: www.elsevier.com/locate/chemphys

Basis set truncation further clarifies vibrational coherence spectra

Daniel B. Turner[a], Paul C. Arpin[b,*]

[a] Micron School for Materials Science and Engineering, Boise State University, Boise, ID 83725, USA
[b] Department of Physics, California State University, Chico, Chico, CA 95929, USA

ABSTRACT

Coherent vibrational oscillations in femtosecond transient-absorption spectra have been interpreted since the 1990s using a model based on Gaussian wavepacket dynamics. The oscillations are often studied using probe-wavelength dependent plots of the oscillation amplitude and phase that are known as vibrational coherence spectra. Here we show that restricting the basis of the wavepacket to a small number of eigenstates clarifies several features in vibrational coherence spectra. Improving the understanding of vibrational coherence signatures will help distinguish them from signatures of electronic coherence that arise from measurements of strongly coupled excitonic states in molecular aggregates and light-harvesting proteins.

1. Introduction

A femtosecond laser pulse can excite a nonstationary vibrational wavepacket on the electronic states of molecules. The coherent oscillations of such a wavepacket produce oscillations of the nonlinear optical signal as the delay time between the pump and probe pulses is varied in a time-resolved spectroscopy measurement [1]. In transient-absorption spectroscopy, the amplitude and phase of the observed oscillations vary with probe wavelength, and these features of the oscillations began to be studied intently in the late 1980s [2]. The oscillations were observed in transient-absorption measurements of conjugated laser-dye molecules and pigment–protein complexes throughout the 1990s [3–13], and the effects of pulse chirp on the oscillations were explored [14,15]. Subsequently, Champion and coworkers developed a theoretical framework to model coherent vibrational oscillations in systems having nonradiative decay mechanisms such as nonadiabatic transfer [16]. More recently, researchers have gained a renewed interest in using the coherent wavepackets to resolve the dynamic Stokes shift in pigment–protein complexes and molecules [17–20], to explore coherence in electron-transfer reactions [21], to quantify ultrafast protein solvation dynamics [22], to search for signatures of nonadiabatic dynamics [23,24], to study the excited-state dynamics of a molecule used for the medical application of photodynamic therapy [25], and to characterize the evolution of vibrational coherence in isomerization reactions and electronic internal conversion [26–30]. Other theoretical explorations included broadening the application of the doorway–window approach [31,32] and studying wavepacket dynamics under intense pumping [33]. Cina and coworkers recently presented an edifying theoretical description of the coherent vibrational oscillations in transient–absorption spectra [34]. In these studies, researchers often analyze the probe-wavelength dependence of the coherent wavepacket dynamics in the frequency domain, see Fig. (1), where a Fourier transformation of the oscillatory signal yields a *vibrational coherence spectrum* composed of both amplitude, $A(\lambda)$, and phase, $\phi(\lambda)$, profiles. One appealing aspect of this analysis method is that it isolates the coherent oscillations at a single frequency even when the pump pulse excites multiple Franck–Condon active vibrational modes.

These foundational works revealed two characteristic signatures of coherent vibrational wavepacket dynamics that are readily apparent in a vibrational coherence spectrum. There is an abrupt phase shift of the oscillations as a function of probe wavelength, and the phase shift is accompanied by an amplitude node. These two characteristic features typically appear at the probe wavelength that corresponds to the maximum signal in a steady-state fluorescence spectrum. In previous works, the coherent oscillations were interpreted through a model of coherent wavepacket dynamics [2,4,7,35]. In this description—depicted in the left panel of Fig. (2)—the pump pulse promotes a Gaussian wavepacket to the displaced excited electronic state. The wavepacket then evolves in phase space, oscillating on the excited-state potential energy surface. The probe pulse returns the wavepacket to the ground electronic state resulting in the stimulated emission of a photon. For a conceptual interpretation, this transition is often treated in the classical limit where the emitted photon must have energy equal to the instantaneous gap between the excited and ground electronic states [36,35]. For displaced harmonic oscillator potentials, the energy gap is proportional to the internuclear displacement, q. As the wavepacket evolves, the probe wavelength resolved oscillation spectrum essentially follows the wavepacket: The probe signal increases when the wavepacket is at an internuclear displacement value with a peak at that

* Corresponding author.
E-mail addresses: danielturner926@boisestate.edu (D.B. Turner), parpin@csuchico.edu (P.C. Arpin).

https://doi.org/10.1016/j.chemphys.2020.110948
Received 31 May 2020; Received in revised form 3 August 2020; Accepted 4 August 2020
Available online 08 August 2020

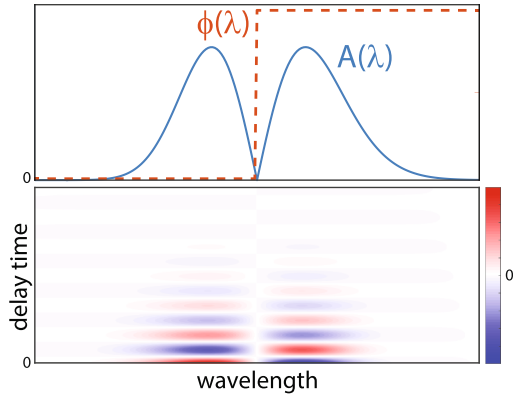

Fig. 1. (bottom) Illustration of oscillatory signals commonly observed in transient-absorption spectroscopy measurements conducted with broadband laser pulses. (top) A *vibrational coherence spectrum* displays the amplitude and phase profiles of the signal at a selected oscillation frequency, which, respectively, reveal the characteristic amplitude node and abrupt π phase shift.

probe energy and decreases when the wavepacket moves to another internuclear displacement value. Considering the wavepacket dynamics from the perspective of a single probe wavelength, as the wavepacket moves in and out of the vicinity of that internuclear displacement value, the signal will increase and decrease. On either side of the minimum of the potential, the wavepacket—because it has some width—will pass through once per oscillation period, yielding an oscillation frequency that matches the vibrational oscillation. At the minimum of the potential, the wavepacket is observed twice per cycle—once passing in each direction—and the stimulated emission signal oscillates at twice the vibrational frequency. Cina and coworkers recently presented a related, qualitative interpretation of the phase flip based on a schematic illustration of the two-dimensional dynamics of a multi-mode vibrational wavepacket in Fig. (11) of Ref. [34]. In particular, their work emphasizes that it is not necessary for the wavepacket to pass through the absolute minimum of the excited state potential during its evolution as the multi-dimensional surface for a molecule with multiple Franck–Condon active vibrational modes contains a locus of points where the potential energy difference is equal to the fluorescence maximum.

While the predictions arising from the full Gaussian wavepacket model are somewhat—but not completely—consistent with laboratory measurements, certain aspects can be difficult to conceptualize. Here we use a basis-set truncation method to offer a complementary explanation of the features in a vibrational coherence spectrum. In particular, we discuss: (i) The presence of a node in the oscillation amplitude. (ii) The presence of an abrupt π change in the oscillation phase. (iii) Both the node and phase shift occur at the wavelength corresponding to the maximum of the steady-state fluorescence spectrum. (iv) The presence of small variations in the phase of the oscillations near—but not at—the amplitude node. (v) Modest asymmetry of the two peak amplitudes.

2. Theory

Here we seek to understand a transient–absorption spectroscopy measurement conducted with broadband laser pulses, in which the pump pulse creates a wavepacket on the excited-state potential energy surface that is a superposition of vibrational eigenfunctions. We choose to use the eigenfunctions of the conventional quantum harmonic oscillator, and, as shown in Fig. (2), we focus on the wavepacket that is on the excited electronic state, $|\psi\rangle = \sum_n c_n |e, n\rangle$, plotted as a function of the displacement, q. Following the Franck–Condon principle, for small displacements, the most significant contributions to the wavepacket will be the two lowest-energy eigenfunctions, $n \in \{0, 1\}$. The two eigenfunctions will interfere, and the superposition will evolve at the fundamental frequency of the mode, ω_0. The two eigenfunctions cannot interfere where one has zero amplitude, and therefore there will be a node in the interference where the $\langle q|e, 1\rangle$ function has zero amplitude. The abrupt π phase change in the oscillations is a consequence of the sign change in $\langle q|e, 1\rangle$. Both the node and phase shift occur at the minimum of the excited-state potential, $q_{\min}$. Below we expand on this swift visual interpretation of the wavepacket in a truncated basis and show how it is consistent with additional features observed in the measured spectra and provides physical insight.

We consider the doorway-window approach [37] for vibrationally abrupt pulses and focus on stimulated emission because the excitation pulse in many measurements has sufficient bandwidth to select primarily for oscillations on the excited electronic state [4,17,20]. This approximation is appropriate when the transition–dipole moment is independent of internuclear displacement value and the pump pulse has a spectrum that encompasses the absorption spectrum [35,34]. We treat the doorway function as the state prepared on the excited electronic state by the pump pulse [36,35] and follow a Franck–Condon approach to calculate a distribution of vibrational eigenfunctions in the electronic excited state due to the instantaneous promotion of a portion of the ground-state eigenfunction to the excited electronic state. We then propagate the wavepacket in the field-free excited-state potential. For convenience and to emphasize the shape, we assume that (1) the system can be represented as a pure state, (2) use a temperature of 0 K, and (3) use a classical window function. We address the quantized window function in Appendix A.

We identify the two electronic states as $|g\rangle$ and $|e\rangle$, each with a progression of vibrational eigenfunctions. We represent the ground state—the lowest-energy vibrational eigenfunction of the ground electronic state—at time zero as $|g, 0\rangle$ and the n^{th} vibrational level of the excited state as $|e, n\rangle$. The density matrix of the ground state in the basis of the displaced excited-state potential at time $t = 0$ when the pump pulse excites the molecule is given by

$$\rho(0) = \sum_{n,n'} c_{n0} c^*_{n'0} \Big| e, n \Big\rangle \Big\langle e, n' \Big|, \tag{1}$$

where the coefficients $c_{ab} = \langle e, a|g, b\rangle$ give the amplitude of each vibrational eigenstate in the excited electronic state. We reserve indices n (m) for the excited (ground) state. The system then evolves on the excited electronic state for time τ, and the density matrix in the q basis is then given by

$$\begin{aligned}\rho(q;\tau) &= \langle q \exp -i\widehat{H}_e \tau \rho(0) \exp +i\widehat{H}_e \tau | q\rangle \\ &= \sum_{n,n'} c_{n0} c^*_{n'0} \exp -i(E_n - E_{n'})\tau \psi_n(q - q_{\min}) \psi^*_{n'}(q - q_{\min}),\end{aligned} \tag{2}$$

where $\widehat{H}_e$ is the nuclear Hamiltonian on the excited electronic state, E_n is the energy of the n^{th} vibrational eigenstate above the minimum of the excited state potential, and the $\psi(q)$ are the vibrational eigenfunctions. In practice, when analyzing coherent vibrational dynamics in a measured transient–absorption spectrum, researchers typically subtract the static and slowly varying signals and then fast Fourier transform the residual oscillations to produce the vibrational coherence spectrum. Hence we focus on the Fourier transform of the density matrix over τ and find

$$\begin{aligned}\tilde{\rho}(q;\omega) &= \mathscr{F}_\tau\{\rho(q;\tau)\} \\ &= \sum_{n,n'} c_{n0} c^*_{n'0} \psi_n(q - q_{\min}) \psi^*_{n'}(q - q_{\min}) \delta(\omega - (E_n - E_{n'})).\end{aligned} \tag{3}$$

This predicts a progression of frequencies for each vibrational mode where the oscillation amplitude and phase are defined at each internuclear displacement value and are determined by sums of products of the time-independent eigenfunctions. To clarify the discussion, we initially treat the ground and excited electronic states as displaced harmonic oscillators, where the energy gap between eigenstates,

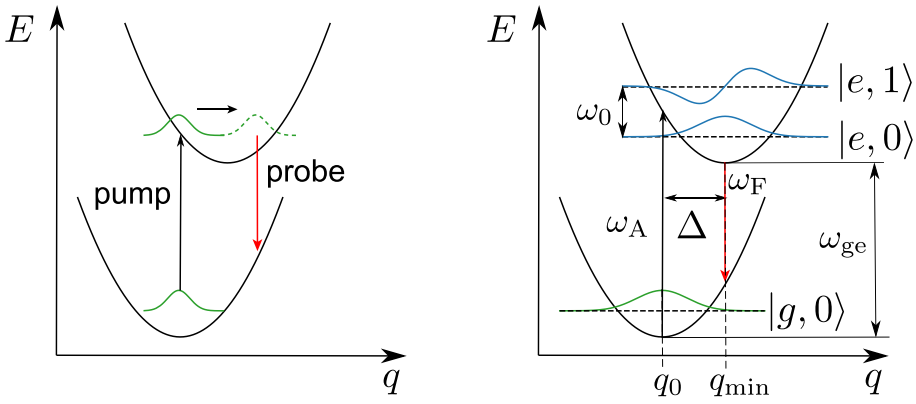

Fig. 2. Wavepacket models. (left) Conventional model is based on evolution of Gaussian wavepacket in the excited state implicitly composed of an infinite number of vibrational eigenfunctions. (right) Trunctating the basis to a limited number of excited-state vibrational eigenfunctions reveals the origin of the amplitude node and phase shift arise in largely from the node and sign change in the $n = 1$ eigenstate. Frequencies ω_A and ω_F are the absorption and fluorescence maxima, respectively, and ω_{ge} is the frequency corresponding to the vertical shift of the excited-state potential. Vibrational frequency ω_0 characterizes the oscillator, and Δ is the displacement.

$E_n - E_{n'} = (n - n')\omega_0$, is constant, where ω_0 is the fundamental frequency of the vibrational mode and $\hbar = 1$. Second harmonic oscillations have been observed in gas-phase transient-absorption measurements of molecular I_2 [35], and were observed to contribute very weakly in a measurement of a condensed-phase sample [25]. Therefore we focus on positive frequency terms that oscillate at the fundamental frequency—meaning only the $n - n' = 1$ terms—and identify the oscillation amplitude for the fundamental frequency, $M^{\mathrm{HO}}(q)$, as

$$M^{\mathrm{HO}}(q) = \sum_{n=1} c_{n0} c^*_{n-1,0} \psi_n(q - q_{\min}) \psi^*_{n-1}(q - q_{\min}). \tag{4}$$

Vibrational coherence spectra are displayed as a function of probe wavelength, λ, and therefore we transform q to λ using the potential-energy difference between the two states, $V_e(q) - V_g(q)$. For the harmonic oscillator, the probe frequency, ω, becomes

$$\begin{aligned}\omega = V_e(q) - V_g(q) &= \underbrace{\omega_{ge} + \tfrac{1}{2}\tfrac{\omega_0}{x_0^2}(q - q_{\min})^2}_{\text{excited state}} - \underbrace{\tfrac{1}{2}\tfrac{\omega_0}{x_0^2}(q - (q_{\min} - \Delta))^2}_{\text{ground state}} \\ &= \omega_F - \tfrac{1}{2}\tfrac{\omega_0}{x_0^2} 2\Delta(q - q_{\min}),\end{aligned} \tag{5}$$

where the classical turning point of the $n = 0$ state is $x_0 = \sqrt{1/m_{\mathrm{eff}}\omega_0}$, m_{eff} is the effective mass of the mode, and we have substituted the peak of the fluorescence spectrum as the frequency at the minimum of the excited-state potential, $\omega_F = \omega_{ge} - \frac{1}{2}\frac{\omega_0}{x_0^2}\Delta^2$. In the simplest case in which only the two lowest-energy vibrational levels are excited on the electronic excited state, we can write the amplitude of the oscillations as a function of probe wavelength, $M^{\mathrm{HO}}_{01}(\lambda)$ as

$$M^{\mathrm{HO}}_{0,1}(\lambda) \propto \frac{1}{\omega_0 \Delta}\left(\frac{1}{\lambda_F} - \frac{1}{\lambda}\right) \exp\left[-\frac{4\pi^2 c^2 x_0^2}{\omega_0^2 \Delta^2}\left(\frac{1}{\lambda_F} - \frac{1}{\lambda}\right)^2\right] \tag{6}$$

The amplitude and phase profiles of the vibrational coherence spectrum as depicted in Fig. (1) are then written as

$$A(\lambda) = |M(\lambda)| \tag{7a}$$

$$\phi(\lambda) = \mathrm{Im}\{\ln(M(\lambda))\}. \tag{7b}$$

3. Results and discussion

A key insight of this work is that the node and phase shift observed in the vibrational coherence spectrum can be understood swiftly using a visual inspection of the two lowest-energy vibrational eigenfunctions of the excited electronic state. As an initial assessment of the validity of this basis-set truncation method, we compare the dynamics of the wavepacket projected into either the complete basis or a truncated basis in Fig. (3). We chose a displacement of $\Delta/x_0 = 0.5$ as a representative example. Normalizing the displacement to the classical turning point yields results that are independent of the oscillator's frequency. We

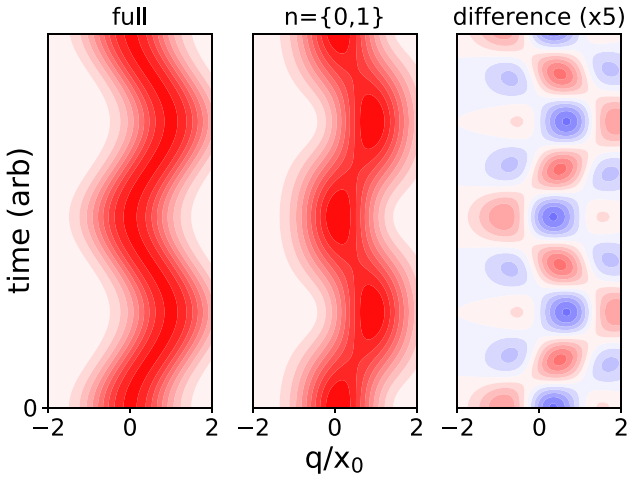

Fig. 3. Comparison of Gaussian wavepacket dynamics in the (left) full and (middle) two-eigenstate bases for $\Delta/x_0 = 0.5$. The structure of the residual in the difference plot (right) strongly resembles the $n = 2$ eigenstate.

compare the wavepacket in the full and two-eigenstate bases in the left ("full") and middle ("$n = \{0, 1\}$") panels, respectively. Visually, the wavepacket dynamics in the two bases are quite similar. Upon closer inspection, the full wavepacket simulation shows smooth transitions between the turning points; in contrast, the two-eigenstate wavepacket has a more choppy oscillation character. The difference between the two—amplified by a factor of 5 in the right panel—demonstrates that the primary missing contribution is the $n = 2$ eigenstate. Inspection of the central panel reveals that, indeed, along $q/x_0 = 0.5$ in this example the amplitude is a constant as a function of time, which will produce the node in the amplitude profile of the vibrational coherence spectrum. The phase difference can be observed by identifying the cosinusoidal character of the time trace for $q/x_0 = 0$ and the sinusoidal character of the time trace at $q/x_0 = 1$, as example. This difference gives rise to the π phase shift in the vibrational coherence spectrum. Finally, the node and change in phase occur both at $q = \Delta$, which is q_{min} in Fig. (2) the minimum of the excited-state potential and will be the maximum of the steady-state fluorescence spectra in this model.

Next we quantify the projection of the wavepacket into various bases. For the full basis, we confirmed that the projection is unity for all values of Δ/x_0. Fig. (4) shows that even for a relatively large displacement value of $\Delta/x_0 = 1$, the projection of the wavepacket into the basis of the two lowest-energy eigenfunctions is greater than 0.9. For displacement values of $\Delta/x_0 \approx 2$, it would be slightly better to use a wavepacket composed of the $n = 1$ and $n = 2$ eigenstates rather than the $n = 0$ and $n = 1$ eigenstates, indicating that the coefficients arising from the projection of the ground state onto the excited-state manifold switch in relative amplitude, $|c_2|^2 > |c_0|^2$, for this range of displacement

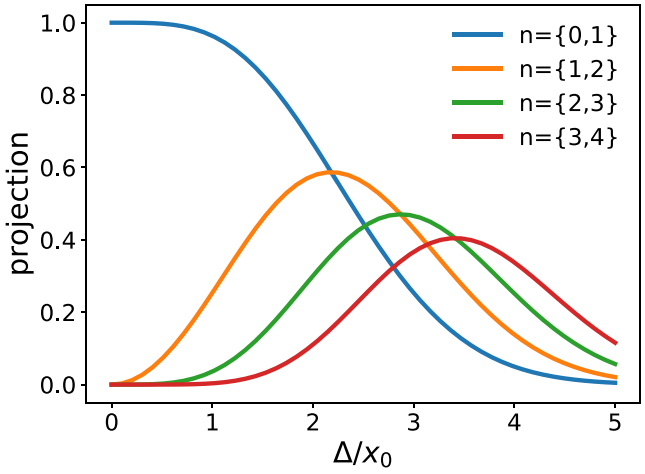

Fig. 4. The projection of the wavepacket onto various two-eigenstate bases. The projection into the $n = \{0, 1\}$ basis is greater than 0.9 until Δ/x_0~1.

values. This small advantage exists again for the pair of $n = \{2, 3\}$ and so forth as the displacement value increased further.

These basic evaluations demonstrate that the key features of the full wavepacket dynamics are reproduced effectively using the lowest two-eigenstate basis, and therefore we next produce and evaluate the vibrational coherence spectra. Specifically we will compare the overall amplitude and width of the oscillations between the two models. Fig. (5) contains a representative example and presents the oscillation

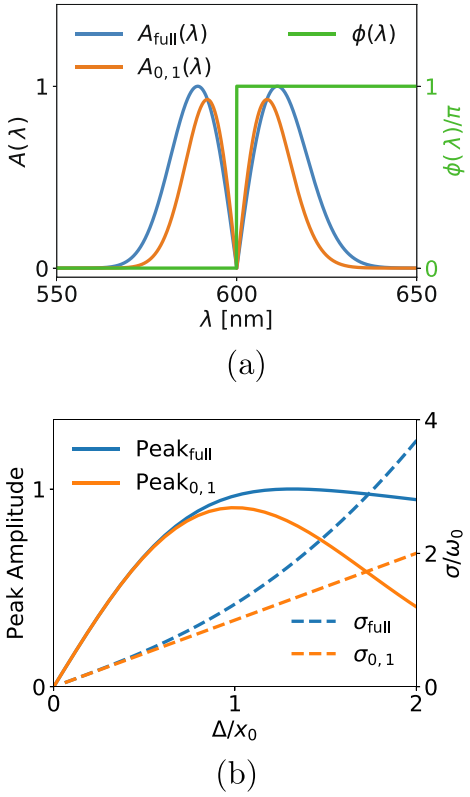

Fig. 5. Vibrational coherence spectra from the wavepacket in the two-eigenstate and full bases. (a) Representative vibrational coherence spectrum for a displacement $\Delta/x_0 = 1$, fluorescence peak $\lambda_F = 600$ nm, and ω_0 corresponding to a 10 THz (300 cm^{-1}) mode. The amplitude profile $A(\lambda)$ is plotted for full model (blue) and two-eigenstate model (orange). The phase profile $\phi(\lambda)$ (green) is identical for both calculations, (b) Peak amplitude and width of the vibrational coherence spectrum as a function of the displacement for full-eigenstate model (blue) and for the two lowest-energy eigenstate model (or- ange).

amplitude and width of the peak of the vibrational coherence spectrum as functions of Δ/x_0.

Fig. (5) presents the vibrational coherence spectrum for $\Delta/x_0 = 1$ for both the full model and the two-eigenstate model. At the large displacement of $\Delta/x_0 = 1$, modest quantitative discrepancies between the two models appear. As the displacement increases, the vibrational coherence spectrum is increasingly composed of higher-energy eigenstates, and therefore the peak amplitude (peak of $A(\lambda)$) of the two-eigenstate model is lower than the infinite eigenstate model. The higher-energy eigenstates have a broader spatial extent, and the width of the two-eigenstate model is visibly smaller. However, the shape is qualitatively similar, and in particular the location of the node and phase change are identical. At the fundamental vibrational frequency, the vibrational coherence spectrum is composed of a sum of pairwise combinations of eigenstates of the harmonic oscillator ($\psi_n\psi_{n+1}$) and the combined even–odd parity gives a node at $q = q_{min}$ for every term in the sum. High-energy pairs (for example {1,2}, {2,3}) have additional nodes in the product eigenstates, but summing over all pairs as shown in Eq. (4) leaves only the one common node at $q = q_{min}$.

In the remainder of Fig. (5) we investigate the primary distinctions—the peak value and the width—between the full wavepacket model and the two-eigenstate wavepacket model. We use Eq. (4) to sum the pairwise contributions where the amplitudes c_n of each state are determined by the overlap integral between the ground state vibrational eigenfunction with the eigenfunctions in the displaced excited state potential. For the two-eigenstate model, we truncate the sum at $n = 1$, for the full model, we use sufficient eigenstates to ensure we preserve the norm of the excited state wavefunction. We normalize the peak value in each case by the maximum reached in the full eigenstate case. The interference terms ($\psi_n\psi_{n+1}$) require a significant amplitude in each eigenstate, and therefore the vibrational coherence spectrum peak value grows for small displacement as the $n = 1$ state increases in amplitude. Near $\Delta/x_0 = 1$ the peak amplitude reaches a maximum as the amplitude is spread over many eigenstates. We emphasize that for $\Delta/x_0 < 0.8$ the two models make nearly identical quantitative predictions. Our metric of Δ/x_0 is closely related to the Huang–Rhys factor, S, $S = (1/2)(\Delta/x_0)^2$. Hence the cut-off value of Δ/x_0~1 corresponds to S~0.5. Using that relation, we compared the results of a joint theory/measurement study [38] and found that of the 25 modes analyzed in their Table S1, most modes had S~0.02 and the largest was S~0.28. This supports the notion that the truncated basis approximation has at least moderate utility in the analysis of laboratory measurements of molecular samples.

Separately, we performed a calculation consistent with the semi-classical Gaussian wavepacket model. We created a Gaussian wavepacket composed of 10^5 point masses with normally distributed initial position and momenta and propagated each classically on the excited-state potential. A fast Fourier transform of the time-dependent wavepacket dynamics produced a peak oscillation amplitude as a function of the initial displacement of the wavepacket. The results (not shown) are identical to the full-eigenstate model shown in Fig. (5).

Next we quantify the width of this unusually shaped amplitude profile. We define the width as $\sigma^2 = \langle\omega^2\rangle - \langle\omega\rangle^2$ and calculate

$$\sigma = \frac{1}{N}\sqrt{\int_{-\infty}^{\infty} A(\omega)\omega^2 d\omega - \left[\int_{-\infty}^{\infty} A(\omega)\omega d\omega\right]^2}, \tag{8}$$

where $N = \sqrt{\int_{-\infty}^{\infty} A(\omega)d\omega}$ is a normalization. This expression is analytic in the two-eigenstate harmonic oscillator basis, and we find $\sigma_{0,1}^{HO} = \omega_0\Delta/x_0$. In Fig. (5) we observe the anticipated behavior for the width of the two-eigenstate model. At large Δ/x_0 the width of the full-eigenstate model increases at a faster rate than the two-eigenstate model.

Short pump pulses typically excite several Franck–Condon active modes in a molecule, where most of this work has considered only a single active mode. In a recent article, Cina and colleagues described how the excitation of several Franck–Condon modes with small

displacements contributes to the overall out-of-phase oscillations on either side of the fluorescence peak observed in the time dependence of transient–transmittance measurements [34]. In Appendix B we analyze the case of an electronic excited state with two Frack–Condon active vibrational modes. We find that the node and phase shift are unchanged, however we find that additional modes increase the width of the amplitude profiles of the vibrational coherence spectra.

In many measurements the amplitude profile of a vibrational coherence spectrum is asymmetric, meaning that the peak on one side of the node has more amplitude than the peak on the other side of the node. Often it is the case that the higher-energy side has more amplitude than the lower-energy side [16,26,17,18,21,22]. This result was not reproduced by any simulations using the harmonic oscillator eigenfunctions. Therefore we hypothesized that an anharmonic oscillator may reproduce the measured asymmetry, as well as, perhaps, the gradual slopes that are oftentimes observed in the phase profiles. We chose to use the Morse oscillator because there are analytic expressions for its eigenfunctions [39] [1] For a diatomic molecule, the Morse oscillator successfully captures the sharp rise in energy at small internuclear separations and the asymptote at large internuclear separations, and this model is harmonic near the equilibrium distance, r_e, and use this to quantify the potential via an effective classical turning point for the lowest-energy state, x_0.

In Fig. (6) we present the two lowest-energy vibrational eigenfunctions, the wavepacket dynamics in the two-eigenstate and full bases, as well as their vibrational coherence spectra. The parameters of this example system were set such that there were 34 bound vibrational eigenstates. Panel (a) shows that the $n = 1$ eigenstate is visually asymmetric as a function of q, and therefore we expect some type of asymmetry to the vibrational coherence spectra. The time-domain plots of the wavepacket in the full and two-eigenstate bases in panel (b) reveal—just like the model using harmonic oscillator—that the major factor missing from the dynamics of the two-eigenstate model is the two-node character of the $n = 2$ eigenstate. Yet the same overall qualitative aspects remain for the Morse oscillator model that existed for the harmonic oscillator model: overall the dynamics are well-reproduced even when the basis is restricted to two eigenstates, the phase shift will arise due to the cosinusoidal and sinusoidal sides of the wavepacket oscillations, and the amplitude node will arise because the equilibrium internuclear displacement value has no oscillation amplitude. Finally, panel (c) displays the vibrational coherence spectra for both the full and two-eigenstate wavepackets. Unlike the analytic solution used to study the harmonic oscillator, here we performed a direct fast Fourier transformation of wavepacket oscillations to produce the vibrational coherence spectra. Both amplitude profiles are asymmetric in width—which primarily arises due to the inversion required to transform from the frequency variable to the wavelength variable—as well as in height—which is far more interesting and results from the anharmonic nature of the potential. To explore the relation between the peak height ratio and the anharmonicity further, we ran a series of simulations at varying amounts of anharmonicity. The data revealed two key results. First, as anharmonicity increased, the relative peak-height difference increased, supporting our conclusion that anharmonicity leads to the difference in peak heights. Second, the vibrational coherence spectra that result from the full and truncated bases began to diverge very slightly as anharmonicity increased. For example, in the case of 66 bound states, the agreement was nearly perfect, whereas for the case of only 7 bound states, minor quantitative differences were visible.

Finally, in Fig. 6, the phase profile of the two-eigenstate wavepacket is flat on either side of the phase shift, which is identical to that of the harmonic oscillator model. In contrast, the phase profile of the

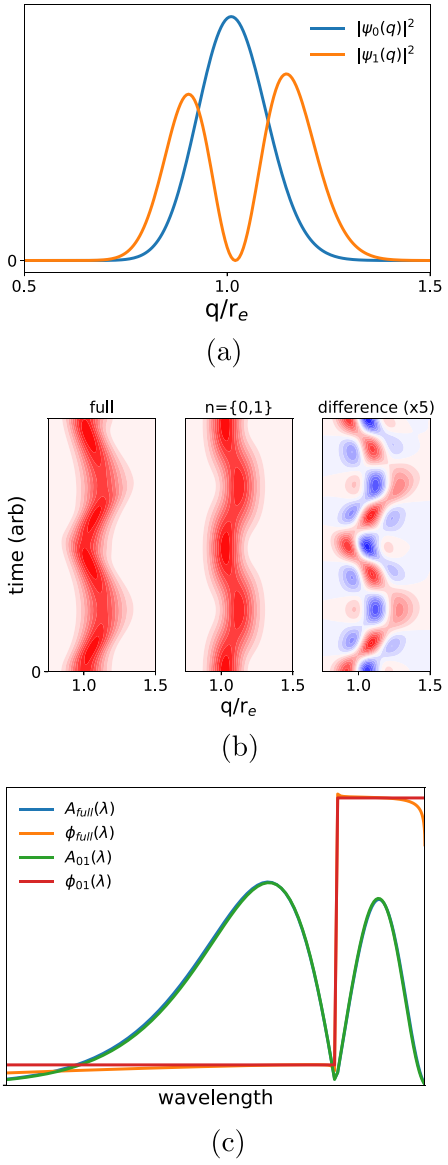

Fig. 6. Results from Morse oscillator for representative set of parameters with 34 bound eigenstates. (a) Two lowest-energy eigenstates of the Morse oscillator reveal asymmetry as function of q, (b) Dynamics of the wavepacket in the full and two-eigenstate bases for $\Delta/x_0 = 0.5$, (c) Vibrational coherence spectra reveal asymmetric heights in the amplitude proles and a gradual slope to the phase as it approaches the π shift for the full wavepacket.

wavepacket in the full basis has some gradual phase changes on either side of the node. These gradual phase changes arise from an indirect effect of the anharmonic potential. The anharmonic potential yields an unequal spacing of energy levels, which leads to a distribution of oscillation frequencies of the wavepacket. Because the oscillations decay—both in the simulation and in molecules measured in the laboratory—the peaks in the frequency domain have non-zero widths and can overlap. This interference yields the gradual phase changes. In a measurement, the gradual phase change could indicate interference from two distinct modes that have similar frequencies or from a single mode that is anharmonic, such as the one modeled here.

The results from the harmonic and Morse oscillator models show that restricting the basis set of the wavepacket to the two lowest-energy eigenfunctions clarifies the origin of the amplitude node and phase shift that are commonly observed in measured vibrational coherence spectra. The models are based on certain approximations, and therefore a few limitations warrant discussion. First, if the bandwidth of the

[1] The expression of the normalization constant, $N(\lambda, n)$, in Eq. (41) of Ref. [39] needs an additional factor of $\sqrt{\alpha}$.

pump pulse does not encompass the absorption profile, coherent wavepackets will be launched on both the excited and ground electronic states. The two wavepackets will both produce coherent oscillations in transient–absorption spectra and likely lead to nodes at both the absorption and fluorescence maxima, with additional phase shifts. The same effects would be observed if the pump pulse were not well-compressed or if the transition–dipole moment were not independent of the internuclear separation, such as Herzberg–Teller coupling [40,41]. Second, we have not addressed more complicated potential energy surfaces, such as those with barriers to photoproduct intermediates [22] or those that induce nonadiabatic transitions resulting from avoided crossings or conical intersections in photochemical reactions [16,42]. Third, the simulations excluded damping arising from a dissipative system–bath interaction [1]. Damping would primarily serve to broaden the peaks along the frequency axis that arise from Fourier transformation of the time-delay variable. For any particular mode, the influence on a vibrational coherence spectrum—which arises typically from a slice at the peak of the amplitude along this frequency axis—is likely to be negligible. However, if a sample had two or more modes of very similar frequencies, damping may cause overlap and interference among the features.

4. Conclusions

We have evaluated the amplitude and phase profiles of vibrational coherence spectra observed in transient absorption spectroscopy, focusing on insights gleaned by truncating the basis of vibrational eigenstates. This description yielded an intuitive picture of the source of the shape of the amplitude and phase profiles, particularly when focusing on only the two lowest-energy vibrational eigenstates. Using anharmonic potentials produced vibrational coherence spectra that were asymmetric in relative peak amplitude, which is a common occurrence in measured spectra. In addition, the models led to predictions about the shape of the vibrational coherence spectrum that could be compared with experimental measurements. These details are a key method by which one can distinguish vibrational coherences from electronic coherences arising from strongly coupled excitonic states in molecular aggregates. This distinction is critical for studies of electronic energy transfer mechanisms in molecular aggregates and photosynthetic light-harvesting proteins.

An ideal molecular sample to which these predictions can be compared would have a high fluorescence quantum yield with minimal photactivity and a large Stokes shift to distinguish clearly the ground-state wavepackets from those on the excited state. Finally, it would be convenient for the molecule to have a limited number of dominant vibrational modes so that excessive post-processing of the dataset is not necessary. Creating a significant signal from excited-state wavepackets and suppressing wavepacket oscillations on the ground state requires a laser pulse shorter than the vibrational period [35], hence an ideal molecule would have an absorption peak and a fluorescence peak in a wavelength range where few-cycle laser pulses are readily produced, typically 500 nm to 800 nm.

CRediT authorship contribution statement

Daniel B. Turner: Conceptualization, Methodology, Formal analysis, Writing - original draft, Writing - review & editing, Visualization. **Paul C. Arpin:** Conceptualization, Methodology, Formal analysis, Writing - original draft, Writing - review & editing, Visualization.

Declaration of Competing Interest

The authors declare that they have no known competing financial interests or personal relationships that could have appeared to influence the work reported in this paper.

Acknowledgements

DBT thanks the Department of the Navy, Office of Naval Research under ONR award number N00014-19–1-2615 for support of this research. We thank Darin Ulness for reviewing an initial draft of the manuscript.

Appendix A. Window in a vibrational eigenstate basis

In posing this model, we have used the doorway-window approach in which we have treated the doorway and time evolution in a vibrational eigenstate basis, but we treated the window classically. We assumed that projecting the wavepacket back into the ground electronic state requires only that the laser energy match the instantaneous energy gap between the ground and excited state potential at the internuclear displacement value of the wavepacket. In other words, we chose a convenient, analytic route for the transformation to Eqns. (7b) because we aimed to study not the full nonlinear optical spectroscopy measurement but rather a key conceptual interpretation.

To provide a more complete model of a transient–absorption spectroscopy measurement, in this Appendix we consider projecting the excited-state wavepacket to the ground electronic state using a window operator represented in a vibrational eigenstate basis. Without line broadening, this leaves only transitions at discrete energies $\omega_{n,m} = E_n - E_m$. The q dependence becomes obscured because the Franck–Condon factor for the transition between any two states is a constant, independent of time. The laser frequency dependence then arises from the sum of, potentially, many contributing $|e, n\rangle \rightarrow |g, m\rangle$ transitions with distinct amplitudes and phases.

We can rewrite the time-dependent density matrix $\rho(\tau)$ from Eq. (2) to exclude the q basis

$$\rho(\tau) = \sum_{n,n'} c_{n0} c_{n'0}^{*} \exp\{-i(n - n')\omega_0 \tau\} \left| e, n\rangle\langle e, n' \right|, \tag{A.1}$$

where we assume harmonic oscillator eigenstates.

We follow prior work—specifically Eq. (3.8a) in Ref. [37]—and assume that the laser pulse duration is short compared to the nuclear oscillations but long compared to the dephasing of the electronic transition; we calculate a bare window operator of the form

$$W(\omega) = \sum_{n,n'} |e, n\rangle\langle e, n'| \times \left[\sum_m c_{nm} c_{n'm}^{*} \left[\frac{1}{\omega - \omega_{n',m} + i\gamma/2} - \frac{1}{\omega - \omega_{n,m} - i\gamma/2} \right] \right], \tag{A.2}$$

where γ is the dephasing rate of the electronic transition. Up to overall constants, the spectrally resolved signal is given by

$$S(\omega;\tau) \propto \mathrm{Tr}[\mathrm{W}(\omega)\rho(\tau)], \tag{A.3}$$

where Tr[...] is the trace evaluated here in a basis of the vibrational eigenstates on the excited electronic state. We find

$$S(\omega;\tau) \propto \sum_{n,n',m} c_{nm}c^*_{n'm}c_{n'0}c^*_{n0}\exp[-i(n'-n)\omega_0\tau] \times \left[\frac{1}{\omega-\omega_{n',m}+i\gamma/2} - \frac{1}{\omega-\omega_{n,m}-i\gamma/2}\right]. \tag{A.4}$$

We choose to focus on the terms oscillating at the fundamental vibrational frequency ($n' = n + 1$). In this case, the vibrational coherence spectrum is given by

$$M(\omega) = \sum_{n,m} c_{nm}c^*_{n+1,m}c_{n+1,0}c^*_{n0}\left[\frac{1}{\omega-\omega_{n+1,m}+i\gamma/2} - \frac{1}{\omega-\omega_{n,m}-i\gamma/2}\right]. \tag{A.5}$$

This is a sum of Lorentzian lines centered on the $|e, n\rangle \rightarrow |g, m\rangle$ transition energies with various amplitudes and phases. The amplitudes are dominated by the overlap integrals c_{nm}.

We compared the calculated vibrational coherence spectrum for the purely vibronic model with the classical window model and found that at large displacements the two spectra overlap very well and at small displacements the classical model predicts a much narrower width. This highlights one of the limitations of any classical interpretation of wavepacket dynamics. For small displacements, the relative variation in $\omega = V_e(q) - V_g(q)$ over the full motion of the wavepacket is less than ω_0, however, from the vibrational eigenstates perspective, the transitions are discrete and, for the harmonic oscillator, are spaced by ω_0.

Appendix B. Two-mode analysis

We consider two vibrational modes on the excited electronic state which lead to a two-dimensional wavepacket on the excited electronic state. In addition to oscillations at the fundamental frequency and overtones of each mode, the wavepacket now includes combination bands composed of sums and differences of the two frequencies, as has been observed in prior multi-mode analyses [43,25]. While the combination bands merit further investigation, we focus the discussion here on the fundamental frequencies to be consistent with the remainder of this work.

The wavefunction is composed of a product of the basis functions of the eigenstates $\psi_n^{(s)}(q_s)$, where we label the different vibrational eigenfunctions and modes with $s = 1$ or 2. While the wavefunctions are independent in an internuclear displacement basis, the difference potential $V_e - V_g$ depends on both modes. For a given value of the laser frequency ω there are many combinations of q_1 and q_2 where $V_e - V_g = \omega$ that must be accounted for to calculate the full contribution to the vibrational coherence spectrum. For the harmonic oscillator case, these points make a straight line through the two-dimensional space so for this case we perform a Radon transform [44] to project the $\boldsymbol{q}$ dependent amplitude profiles along lines of constant ω. As an example we calculate the mode amplitude profile at the fundamental frequency ω_1 of the $s = 1$ mode as a function of laser frequency assuming that only the lowest energy vibrational eigenstates needed to create the coherence contribute to the signal and find

$$M(\omega) \propto \frac{\omega_1\zeta_1}{\omega_2^2\zeta_2^2x_2}\sqrt{1+\left(\frac{\omega_1\zeta_1x_2}{\omega_2\zeta_2x_1}\right)^2}\left(1+\left(\frac{\omega_1\zeta_1}{\omega_2\zeta_2}\right)^2\right)^{-3/2} \times (\omega-\omega_F)\exp\left[-\frac{1}{(\zeta_2\omega_2)^2+(\zeta_1\omega_1)^2}(\omega-\omega_F)^2\right], \tag{B.1}$$

where ω_s and x_s are the fundamental frequency and classical turning point of the s vibrational mode and the normalized displacement $\zeta_s = \Delta_s/x_s$ is defined for convenience. We highlight that the general form of the equation is unchanged, but the width of the vibrational coherence spectrum is increased due to the additional mode. A more thorough treatment could consider the details of the shape as additional eigenstates are included.

References

[1] S. Mukamel, Principles of Nonlinear Optical Spectroscopy, Oxford University Press, New York, 1995.

[2] H.L. Fragnito, J.-Y. Bigot, P.C. Becker, C.V. Shank, Evolution of the vibronic absorption spectrum in a molecule following impulsive excitation with a 6 fs optical pulse, Chem. Phys. Lett. 160 (2) (1989) 101–104.

[3] C.J. Bardeen, Q. Wang, C.V. Shank, Selective excitation of vibrational wave packet motion using chirped pulses, Phys. Rev. Lett. 75 (19) (1995) 3410–3413, https://doi.org/10.1103/PhysRevLett.75.3410.

[4] W.T. Pollard, H.L. Fragnito, J.-Y. Bigot, C.V. Shank, R.A. Mathies, Quantum-mechanical theory for 6 fs dynamic absorption spectroscopy and its application to nile blue, Chem. Phys. Lett. 168 (3-4) (1990) 239–245, https://doi.org/10.1016/0009-2614(90)85603-A.

[5] W.T. Pollard, S.-Y. Lee, R.A. Mathies, Wave packet theory of dynamic absorption spectra in femtosecond pump-probe experiments, J. Chem. Phys. 92 (7) (1990) 4012–4029.

[6] W.T. Pollard, R.A. Mathies, Analysis of femtosecond dynamic absorption spectra of nonstationary states, Annu. Rev. Phys. Chem. 43 (1992) 497–523, https://doi.org/10.1146/annurev.pc.43.100192.002433.

[7] M.H. Vos, F. Rappaport, J.-C. Lambry, J. Breton, J.-L. Martin, Visualization of coherent nuclear motion in a membrane protein by femtosecond spectroscopy, Nature 363 (1993) 320–325, https://doi.org/10.1038/363320a0.

[8] N. Scherer, D.M. Jonas, G.R. Fleming, Femtosecond wave packet and chemical reaction dynamics of iodine in solution: Tunable probe study of motion along the reaction coordinate, J. Chem. Phys. 99 (1) (1993) 153–168.

[9] M. Chachisvilis, T. Pullerits, M.R. Jones, C.N. Hunter, V. Sundström, Vibrational dynamics in the light-harvesting complexes of the photosynthetic bacterium Rhodobacter sphaeroides, Chem. Phys. Lett. 224 (1994) 345–351.

[10] Q. Wang, R.W. Schoenlein, L.A. Peteanu, R.A. Mathies, C.V. Shank, Vibrationally coherent photochemistry in the femtosecond primary event of vision, Science 266 (5184) (1994) 422–424, https://doi.org/10.1126/science.7939680.

[11] M. Chachisvilis, H. Fidder, T. Pullerits, V. Sundström, Coherent nuclear motions in light-harvesting pigments and dye molecules, probed by ultrafast spectroscopy, J. Raman Spectrosc. 26 (1995) 513–522, https://doi.org/10.1002/jrs.1250260706.

[12] T.-S. Yang, M.-S. Chang, R. Chang, M. Hayashi, S.H. Lin, P. Vöhringer, W. Dietz, N. Scherer, Femtosecond pump-probe study of molecular vibronic structures and dynamics of a cyanine dye in solution, J. Chem. Phys. 110 (24) (1999) 12070–12081.

[13] F. Rosca, A.T.N. Kumar, D. Ionascu, T. Sjodin, A.A. Demidov, P.M. Champion, Wavelength selective modulation in femtosecond pump–probe spectroscopy and its application to heme proteins, J. Chem. Phys. 114 (2001) 10884, https://doi.org/10.1063/1.1363673.

[14] D.M. Jonas, S.E. Bradforth, S.A. Passino, G.R. Fleming, Femtosecond wavepacket spectroscopy: Influence of temperature, wavelength, and pulse duration, J. Phys. Chem. 99 (9) (1995) 2594–2608, https://doi.org/10.1021/j100009a018.

[15] A. Wand, S. Kallush, O. Shoshanim, O. Bismuth, R. Kosloff, S. Ruhman, Chirp effects on impulsive vibrational spectroscopy: a multimode perspective, Phys. Chem. Chem. Phys. 12 (9) (2010) 2149–2163, https://doi.org/10.1039/b920356g.

[16] A.T.N. Kumar, F. Rosca, A. Widom, P.M. Champion, Investigations of amplitude and phase excitation profiles in femtosecond coherence spectroscopy, J. Chem. Phys. 114 (2001) 701–724, https://doi.org/10.1063/1.1329640.

[17] S.D. McClure, D.B. Turner, P.C. Arpin, T. Mirkovic, G.D. Scholes, Coherent oscillations in the PC577 cryptophyte antenna occur in the excited electronic state, J. Phys. Chem. B 118 (5) (2014) 1296–1308, https://doi.org/10.1021/jp411924c.

[18] P.C. Arpin, D.B. Turner, S.D. McClure, C.C. Jumper, T. Mirkovic, J.R. Challa, J. Lee, C.Y. Teng, B.R. Green, K.E. Wilk, P.M.G. Curmi, K. Hoef-Emden, D.W. McCamant, G.D. Scholes, Spectroscopic studies of cryptophyte light harvesting proteins: Vibrations and coherent oscillations, J. Phys. Chem. B 119 (31) (2015)

10025–10034, https://doi.org/10.1021/acs.jpcb.5b04704.
[19] C.C. Jumper, P.C. Arpin, D.B. Turner, S.D. McClure, S. Rafiq, J.C. Dean, J.A. Cina, P.A. Kovac, T. Mirkovic, G.D. Scholes, Broadband pump-probe spectroscopy quantifies ultrafast solvation dynamics of proteins and molecules, J. Phys. Chem. Lett. 7 (2016) 4722–4731, https://doi.org/10.1021/acs.jpclett.6b02237.
[20] L.A. Bizimana, J. Epstein, D.B. Turner, Inertial water response dominates protein solvation dynamics, Chem. Phys. Lett. 728 (2019) 1–5, https://doi.org/10.1016/j.cplett.2019.04.069.
[21] S. Rafiq, J.C. Dean, G.D. Scholes, Observing vibrational wavepackets during an ultrafast electron transfer reaction, J. Phys. Chem. A 119 (2015) 11837–11846.
[22] L.A. Bizimana, J. Epstein, J. Brazard, D.B. Turner, Conformational homogeneity in the P_r isomer of phytochrome Cph1, J. Phys. Chem. B 121 (12) (2017) 2622–2630, https://doi.org/10.1021/acs.jpcb.7b02180.
[23] V. Tiwari, W.K. Peters, D.M. Jonas, Electronic resonance with anticorrelated pigment vibrations drives photosynthetic energy transfer outside the adiabatic framework, Proc. Natl. Acad. Sci. 110 (4) (2013) 1203–1208, https://doi.org/10.1073/pnas.1211157110.
[24] J. Brazard, L.A. Bizimana, T. Gellen, W.P. Carbery, D.B. Turner, Experimental detection of branching at a conical intersection in a highly fluorescent molecule, J. Phys. Chem. Lett. 7 (1) (2016) 14–19, https://doi.org/10.1021/acs.jpclett.5b02476.
[25] J.C. Dean, S. Rafiq, D.G. Oblinksy, E. Cassette, C.C. Jumper, G.D. Scholes, Broadband transient absorption and two-dimensional electronic spectroscopy of methylene blue, J. Phys. Chem. A 119 (34) (2015) 9098–9108, https://doi.org/10.1021/acs.jpca.5b06126.
[26] A. Kahan, O. Nahmias, N. Friedman, M. Sheves, S. Ruhman, Following photo-induced dynamics in bacteriorhodopsin with 7-fs impulsive vibrational spectroscopy, J. Am. Chem. Soc. 129 (3) (2007) 537–546.
[27] M. Liebel, P. Kukura, Broad-band impulsive vibrational spectroscopy of excited electronic states in the time domain, J. Phys. Chem. Lett. 4 (2013) 1358–1364, https://doi.org/10.1021/jz4004203.
[28] M. Liebel, C. Schnedermann, G. Bassolino, G. Taylor, A. Watts, P. Kukura, Direct observation of the coherent nuclear response after the absorption of a photon, Phys. Rev. Lett. 112 (2014) 238301.
[29] M. Liebel, C. Schnedermann, T. Wende, P. Kukura, Principles and applications of broadband impulsive vibrational spectroscopy, J. Phys. Chem. A 119 (36) (2015) 9506–9517, https://doi.org/10.1021/acs.jpca.5b05948.
[30] P.J.M. Johnson, A. Halpin, T. Morizumi, V.I. Prokhorenko, O.P. Ernst, R.J.D. Miller, Local vibrational coherences drive the primary photochemistry of vision, Nat. Chem. 7 (2015) 980–986, https://doi.org/10.1038/nchem.2398.
[31] M.F. Gelin, D. Egorova, A.V. Pisliakov, W. Domcke, Unified description of sequential and coherent contributions to time-resolved spontaneous emission signals: generalized doorway–window approach, Chem. Phys. Lett. 391 (4–6) (2004) 234–242, https://doi.org/10.1016/j.cplett.2004.05.018.
[32] M.F. Gelin, D.S. Kosov, Doorway–window description of sequential three-pulse photon echo signals, Chem. Phys. 347 (2008) 177–184.
[33] D. Egorova, M.F. Gelin, M. Thoss, H. Wang, W. Domcke, Effects of intense femtosecond pumping on ultrafast electronic-vibrational dynamics in molecular systems with relaxation, J. Chem. Phys. 129 (2008) 214303.
[34] J.A. Cina, P.A. Kovac, C.C. Jumper, J.C. Dean, G.D. Scholes, Ultrafast transient absorption revisited: Phase-flips, spectral fingers, and other dynamical features, J. Chem. Phys. 144 (2016) 175102.
[35] D.M. Jonas, G.R. Fleming, Vibrationally abrupt pulses in pump-probe spectroscopy, in: M.A. El-Sayed, I. Tanaka, Y. Molin (Eds.), Ultrafast Processes in Ultrafast Processes in Chemistry and Photobiology, Chemistry for the 21st Century, Blackwell Scientific Publications, Oxford, 1995, p. 225.
[36] Y.J. Yan, L.E. Fried, S. Mukamel, Ultrafast pump-probe spectroscopy: femtosecond dynamics in Liouville space, J. Phys. Chem. 93 (25) (1989) 8149–8162, https://doi.org/10.1021/j100362a006.
[37] Y.J. Yan, S. Mukamel, Femtosecond pump-probe spectroscopy of polyatomic molecules in condensed phases, Phys. Rev. A 41 (1990) 6485–6504, https://doi.org/10.1103/PhysRevA.41.6485.
[38] G. Lee, J. Kim, S.Y. Kim, D.E. Kim, T. Joo, Vibrational spectrum of an excited state and huang–rhys factors by coherent wave packets in time-resolved fluorescence spectroscopy, ChemPhysChem 18 (2017) 670–767, https://doi.org/10.1002/cphc.201601295.
[39] J.P. Dahl, M. Springborg, The Morse oscillator in position space, momentum space, and phase space, J. Chem. Phys. 88 (7) (1988) 4535–4547, https://doi.org/10.1063/1.453761.
[40] Y. Tanimura, S. Mukamel, Temperature dependence and non-Condon effects in pump-probe spectroscopy in the condensed phase, J. Opt. Soc. Am. B 10 (12) (1993) 2263–2268, https://doi.org/10.1364/JOSAB.10.002263.
[41] H. Kano, T. Saito, T. Kobayashi, Observation of Herzberg-Teller-type wave packet motion in porphyrin J-aggregates studied by sub-5-fs spectroscopy, J. Phys. Chem. A 106 (2002) 3445–3453.
[42] M. Kowalewski, B.P. Fingerhut, K.E. Dorfman, K. Bennet, S. Mukamel, Simulating coherent multidimensional spectroscopy of nonadiabatic molecular processes: from the infrared to the x-ray regime, Chem. Rev. 117 (2017) 12165–12226.
[43] C.A. Farfan, D.B. Turner, Interference among multiple vibronic modes in two-dimensional electronic spectroscopy, Mathematics 8 (2020) 157, https://doi.org/10.3390/math8020157.
[44] J. Radon, On the determination of functions from their integral values along certain manifolds, IEEE Trans. Med. Imaging M1–5 (4) (1986) 170–176.